Combined First-Principles and Experimental Study on the Microstructure and Mechanical Characteristics of the Multicomponent Additive-Manufactured Ti−35Nb−7Zr−5Ta Alloy

Irina Yu. Grubova,* Roman A. Surmenev, Erik C. Neyts, Andrey V. Koptyug, Anastasia P. Volkova, and Maria A. Surmeneva

Read Online

ACCESS | Metrics & More | Article Recommendations | Supporting Information

ABSTRACT: New β-stabilized Ti-based alloys are highly promising for bone implants, thanks in part to their low elasticity. The nature of this elasticity, however, is as yet unknown. We here present combined first-principles DFT calculations and experiments on the microstructure, structural stability, mechanical characteristics, and electronic structure to elucidate this origin. Our results suggest that the studied β Ti−35Nb−7Zr−5Ta wt % (TNZT) alloy manufactured by the electron-beam powder bed fusion (E-PBF) method has homogeneous mechanical properties (H = 2.01 ± 0.22 GPa and E = 69.48 ± 0.03 GPa) along the building direction, which is dictated by the crystallographic texture and microstructure morphologies. The analysis of the structural and electronic properties, as the main factors dominating the chemical bonding mechanism, indicates that TNZT has a mixture of strong metallic and weak covalent bonding. Our calculations demonstrate that the softening in the Cauchy pressure (C' = 98.00 GPa) and elastic constant $\overline{C}_{44}$ = 23.84 GPa is the origin of the low elasticity of TNZT. Moreover, the nature of this softening phenomenon can be related to the weakness of the second and third neighbor bonds in comparison with the first neighbor bonds in the TNZT. Thus, the obtained results indicate that a carefully designed TNZT alloy can be an excellent candidate for the manufacturing of orthopedic internal fixation devices. In addition, the current findings can be used as guidance not only for predicting the mechanical properties but also the nature of elastic characteristics of the newly developed alloys with yet unknown properties.
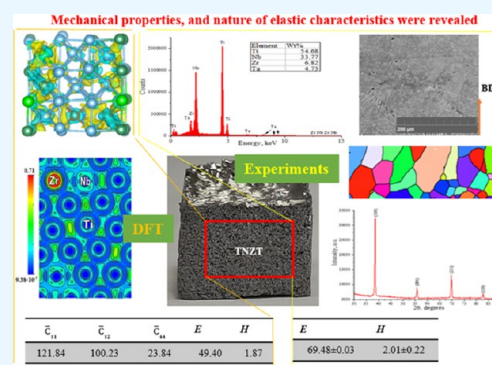
INTRODUCTION

Nowadays, the restoration of large bone defects resulting from high-energy traumatic injuries, tumor resection, diseases, or revision surgery remains an urgent medical and social problem, despite the huge number of available implantation materials. There are disadvantages of the existing load-bearing implant materials such as the content of allergic or cytotoxic elements, which can result in long-term health problems like osteomalacia, peripheral neuropathy, and Alzheimer's diseases,[1] and the so-called "stress shielding effect" caused by the significant difference in Young's modulus (E) between the replacement (∼110 GPa for TiAl$_6$V$_4$) and human bone (10−30 GPa).[2] This effect can potentially lead to bone resorption and eventual implant failure.[3] Due to these issues, there has been an increasing interest in developing new nontoxic biomedical alloys with controlled elastic properties. Moreover, this interest is expected to rise in the next decades with further achievements in the field of alloy manufacturing, material characterization techniques, and computational approaches.[4] Additive manufacturing (AM) is one of the quite advantageous methods for implant production, allowing for better functionalization and production of the case- and patient-specific

implants. Unfortunately, the availability of adequate processes for biocompatible metallic materials is an additional challenge.[5] Experimental investigations of titanium (Ti) and its alloys have shown β-type Ti-based systems with a body-centered cubic (bcc) crystal structure consisting of nontoxic alloying elements (so-called β-stabilizers, such as Nb, Mo, Ta, etc.), which in turn result in reduced E values (∼40−80 GPa), are promising candidates that can indeed decrease the imbalance in the load distribution at the bone-implant contact area, preventing the destructive changes in bone tissues and minimizing the risk of postoperative complications.[6] In addition, despite the fact that Zr is a so-called neutral element, it was observed that it acts as a rather strong β-stabilizer for Ti alloys when used in combination with other β stabilizers such as Ta and Nb.[7,8]

Moreover, the addition of biocompatible Zr provides improved blood circulation in the implant vicinity and enhanced corrosion resistance for β-type Ti implants.[9−13]

Potential β-type Ti-based compositions, such as Ti−30Nb−4Sn,[14,15] Ti−35Nb,[16−19] Ti−15Mo,[20−23] Ti−Nb−Ta,[8,12,24] Ti−24Nb−4Zr−8Sn,[25−30] Ti−12Mo−6Zr−2Fe (TMZF),[31] Ti−15Mo−3Nb−3O (TIMETAL 21SRx),[32] and Ti−13Nb−13Zr,[33] and multicomponent β TNZT attracted great attention due to their reduced elastic modulus, high strength, good corrosion resistance, and superior biocompatibility in comparison with other alloys.[34−37]

Although the extrinsic elasticity of real materials strongly depends on the presence and propagation of dislocations, grain boundaries, cracks, and other defects of the microstructure, the intrinsic elasticity is controlled by the interatomic chemical bonding of the crystal structure. However, the fundamental understanding of the mechanism that governs the decrease in Young's modulus values of β-Ti alloys is still under investigation.

In the past decade, theoretical studies and modeling have become powerful tools for predicting elastic properties and phase stability of multicomponent β-type Ti alloys with the help of first-principles calculations based on density functional theory (DFT). The advantages of modern computer modeling provide insight into the nature of the material's properties and guide experimental studies, eliminating the need for multiple trial-and-error attempts.

Despite the fact that β-Ti-based biocompatible alloys have been extensively studied by a variety of experimental techniques, only a few theoretical studies on the properties of such materials have so far been reported. So far, only the computer simulations based on a first-principles approach can predict the Ti subnanometer physics. Therefore, here we present the discussion of the current state in the field of modeling Ti alloys for a better understanding of the main principles of the design of Ti-based alloys having the lowest possible elastic modulus.

Kuroda et al.[38] proposed a method for the theoretical design of alloys using the theory of molecular orbits. The authors offered a list of theoretically modeled β-Ti alloys with predicted elastic properties and phase stability by using two electronic parameters, viz. "B_o" (bond order) and "M_d" (metal d-orbital energy level). Then, Abdel-Hadi et al.[39] extended this method by combining the deformation mechanism with the composition on the $\bar{B}_o - \bar{M}_d$ diagram. Hennig et al.[40] used ab initio calculations for the investigation of the alloying element effect (including interstitial O, N, and C and substitutional Al and V) on the α to ω martensitic transformation in Ti. It was shown that the β stabilizing effect of Zr enhanced with an increase in Nb concentration in the alloy.[41] Ikehata et al.[42] predicted Young's modulus of the binary Ti$(1−x)$Mx alloy (where M is V, Nb, Ta, Mo, and W) for x = 0, 0.25, 0.75, and 1.0 using a first-principles approach. It was determined that the lowest modulus of elasticity has an alloy with x equal to 0.25. Recently, Dai et al. examined the effect of various alloying elements (Al, Cr, Cu, Fe, Mo, Nb, Ni, Sn, Ta, V, W, and Zr) in binary Ti alloys on the elastic properties, phase stability, and transformation.[43] The same character of the relationship between the formation energy and the content of alloying atoms in the β, α', α'', and ω phases was observed. The addition of all studied alloying elements led to the stabilization of the β, α', and α'' phases, but only Al and Sn increased the stability of the ω phase.[43] Raabe et al.[44] also used ab initio

calculations in combination with experimental data to obtain the optimal approach for creating new biocompatible alloys based on β-Ti with low values of Young's modulus. Sun et al.[45] performed a first-principles study on phase stability, electronic characteristics, and elastic properties of various phases, such as β, α'', and ω for the binary Ti−Nb alloy (25 atom % Nb). It was reported that this β-Ti alloy is the most stable and demonstrates the lowest Young's modulus value in comparison with other binary alloys containing metastable ω and α'' phases. The authors of ref 46 investigated the phase stability and Young's modulus of binary Ti−Nb and ternary Ti−Nb−Zr systems by means of the first-principles calculation. It was shown that binary Ti−25 atom % Nb and ternary Ti−25 atom % Nb−6.25 atom % Zr alloys have a stable β-phase with a low modulus of elasticity and, thus, are suitable for biomedical applications. The results of ref 47 based on the first-principles study of the crystallographic structure and electronic properties of Ti−xNb alloys (x < 50 atom %) have shown that when the content of Nb is low, the hexagonal $\alpha'− \omega$ phases dominate. When the Nb content is more than 18.75 atom %, the β-phase becomes dominant. Huang et al.[48] investigated the effect of temperature on the relative phase stability for the Ti−X (X = 3d, 4d, and 5d elements of the group) alloys in the α, β, and ω phases. Based on theoretical calculations, Hu et al.[49] reported that alloying elements affect phase stability and Young's modulus in Ti alloys.

While the theoretical and experimental investigations of binary and ternary Ti-based alloys are rather well represented in publications, there are very few reports of the ab initio studies investigating the multicomponent novel low-modulus β-type TNZT alloys quite promising for biomedical applications. Moreover, to our knowledge, there is only one experimental work of the TNZT alloy manufactured by selective E-PBF.[50] However, it is of significance to explore the nature of its low elasticity based on the analysis of its electronic structure and atomic bonding.

The combination of first-principles DFT calculations and experimental studies is important for several reasons. By integrating theoretical calculations with experimental investigations, a more comprehensive understanding of the multicomponent TNZT alloy can be achieved. DFT calculations provide insights into the microstructure, structural stability, mechanical characteristics, and electronic structure at the atomic and electronic levels. This complements the experimental studies, allowing for a deeper understanding of the alloy's properties.

In addition, the use of DFT calculations enables the prediction of material properties and behavior, providing valuable guidance for alloy design. Furthermore, experimental studies serve as a crucial validation and verification tool for theoretical predictions. By comparing the results obtained from DFT calculations with the experimental findings, researchers can assess the accuracy and reliability of the theoretical models. This helps to build confidence in the theoretical approach and ensure that the predicted properties align with the observed behavior. Moreover, integrating theoretical calculations with experiments allows researchers to reduce the need for extensive experimental screening and testing. By obtaining preliminary insights and predictions through DFT calculations, researchers can focus their experimental efforts on the most promising alloy compositions and conditions. This leads to improved efficiency and cost reduction in the alloy development process. Finally, the combination of theoretical and experimental

approaches promotes scientific advancement in the field of material science, leading to a deeper understanding of the underlying principles governing the alloy's properties, and opening up possibilities for developing new materials with tailored properties and enhanced performance.

In this context, our purpose is to conduct combined first-principles DFT calculations and experimental studies of the microstructure, structural stability, mechanical characteristics, and electronic structure of the multicomponent TNZT alloy. These results exhibit the origin of the low Young's modulus in TNZT and establish guidance for predicting the mechanical properties of the manufactured alloys based on their elemental composition.

■ THEORETICAL METHODS AND EXPERIMENTAL PROCEDURES

Fabrication of the Samples. The TNZT samples were prepared from a spherical pre-alloyed powder supplied by Tosh SMD Inc. (Grove City, Pennsylvania) using an electron-beam melting Arcam A2 electron-beam melting (EBM) machine (GE Additive, Mölnlycke, Sweden). The TNZT powder particles have a spherical or nearly spherical shape with a small number of satellites, a typical particle diameter range of $1-120$ μm, and an average particle size of 14.7 μm. Particle size distribution of as-received TNZT powder has the following characteristics: D10 = 115 μm − 10%, D50 = 45 μm − 50%, and D90 = 9 μm − 90%. The detailed characterization of the powder properties was reported in detail elsewhere.[51]

Cuboid test samples with the dimensions of about 10 × 10 × 10 mm^3 were manufactured using the following processing parameters: the thickness of the layer (δ) was 100 μm, process temperature (T) settings (initial start plate preheat and process target temperatures) varied from 520 to 610 °C, beam current (I) was 3 mA, beam velocity (v) was 407 mm/s, line offset (h, spacing between hatch lines in a raster type scan) was 0.1 mm, and area energy (E_A) was 4.4 J/mm^2. These settings provided the best physical and mechanical characteristics of the fabricated samples and were set based on the previously reported results.[50] That study was mainly focused on the effects of high-current pulsed electron-beam (PEB) treatment as a surface finishing procedure on the TNZT alloy produced by E-PBF. The changes in the microstructure, crystallite orientation, mechanical properties, and corrosion resistance of the TNZT alloy before and after PEB treatment were assessed. Our previous study has shown that PEB treatment is a viable approach to improve the surface topography of the TNZT alloy while maintaining essential mechanical parameters.

Sample Characterization. The samples of the TNZT alloy for further studies were encapsulated into epoxy resin (Technovit EPOX, Heraeus Kulzer, Wehrheim, Germany) and prepared for investigation using a grinding and polishing machine (Saphir 320, ATA, Mammelzen, Germany). Ti alloys were consistently polished with wet # 60, 320, 600, 800, 1200 to 2000 grits SiC disks. The lapping pressure was 10−20 kPa, and the duration was varied from 2 to 3 min. Further, prior to the final ion peening (Technoorg Linda SEMPrep2 ion mill, Technoorg Linda Co. Ltd., Budapest, Hungary), the sample surfaces were mechanically polished to a mirror finish with the 0.06 μm suspension, followed by 1 ml of a colloidal quartz col-k (nc) suspension at the final polishing step. Polished surfaces are parallel to the build direction (BD), e.g., normal to the

layer plane, and are offset a few mm from the sample sides, avoiding the edge effects.

Scanning electron micrographs obtained in the secondary electron (SE) and backscattered electron (BSE) modes and surface elemental composition were studied with a scanning electron microscope (TESCAN ORSAY HOLDING, Brno, Czech Republic) equipped with an energy-dispersive X-ray (EDX) spectrometer (Oxford Instruments). To characterize the texture of the samples, electron backscatter diffraction (EBSD) measurements were performed using a Tescan MIRA 3 LMU system equipped with an Oxford detector for EBSD. The EBSD mapping was conducted with a scanning step size of 1 μm.

The phase composition of the alloy was determined from X-ray diffraction (XRD) patterns measured with Cu Kα radiation (λ = 1.5406 Å, voltage = 40 kV, and current = 30 mA) in the regular 2θ range from 10 to 90° with the scanning speed of 10°/min using an X-ray diffractometer (Shimadzu XRD-7000S, Japan).

Vickers nanohardness measurements of the cross-sectional TNZT surfaces were performed using a Shimadzu DUH-211S dynamic ultra microhardness tester (Shimadzu, Japan), with the maximum applied load of 30 mN during 10 s. A series of indents, ranging from three to six, were made along the BD with a step size of 100 μm. The indentation process started at a distance of 30 μm from the top edge.

Computational Methods. The VASP 5.4 (Vienna Ab initio Simulation Package) software package was employed to investigate the TNZT system characteristics.[52−56] All calculations were carried out using the projection-augmented wave (PAW) method[56,57] with the generalized gradient approximation (GGA) following the approach by Perdew, Burke, and Ernzerhof (PBE)[58,59] for describing the exchange-correlation functional. The plane wave cutoff energy was fixed at 600 eV. The Brillouin zone sampling was performed by using a 9 × 9 × 9 Monkhorst−Pack k-points grid.[60] The full geometry optimization was performed at a fixed volume of the supercell until the maximum force on each atom was smaller than 0.01 eV/Å. The number of valence electrons in the pseudopotentials was 10 ($3d^34s^1$), 11 ($4p^85s^14d^2$), 12 ($4s^24p^65s^24d^2$), and 5 ($6s^25d^3$) for Ti, Nb, Zr, and Ta, respectively. A 3 × 3 × 3 supercell of Ti−24Nb−5Zr−2Ta atom % (Ti-37, Nb-13, Ta-1, and Zr-3 atoms), with a bcc structure (Im$\bar{3}$m, No. 229), containing in total 54 atoms was used. In the detailed analysis, we only considered the energetically favored configuration of the alloy; local arrangements of atoms yielding minimal changes in the total energy of the studied systems were not taken into account.

The phase stability was estimated by the calculation of the formation (E_f) and cohesion (E_{coh}) energies according to the approach described in ref 61. The elastic constants were calculated in VASP after the geometry optimization of the structure was carried out using the following key tags in the INCAR file: IBRION = 6, ISIF = 7, and NFREE = 2. The elastic constants are calculated from the strain versus stress dependences by specifying six finite lattice distortions with a step size of ± 0.015 Å.[62] The bulk modulus (B), shear modulus (G), and Young's modulus (E_{DFT}) were determined using Voigt−Reuss−Hill approximations.[63] The electron structure was analyzed using charge density difference (CDD),[64] Bader charge,[65] electron localization function (ELF), and density of states (DOS).[66] The thermodynamic properties of the TNZT alloy were represented by corresponding melting point

temperature,[67] Debye temperature, and minimal thermal conductivity, which were calculated based on the values of shear sound velocity (v_s), longitudinal sound velocity (v_l), and average wave velocity (v_m), as suggested in ref 68, 69. The atomic structures in this work were visualized using the VESTA-3 program.[70]

RESULTS AND DISCUSSION

The SE image mode of the SEM micrograph reveals a rather uniform surface topography and morphology of the as-built TNZT specimens (Figure 1a). A small amount of external
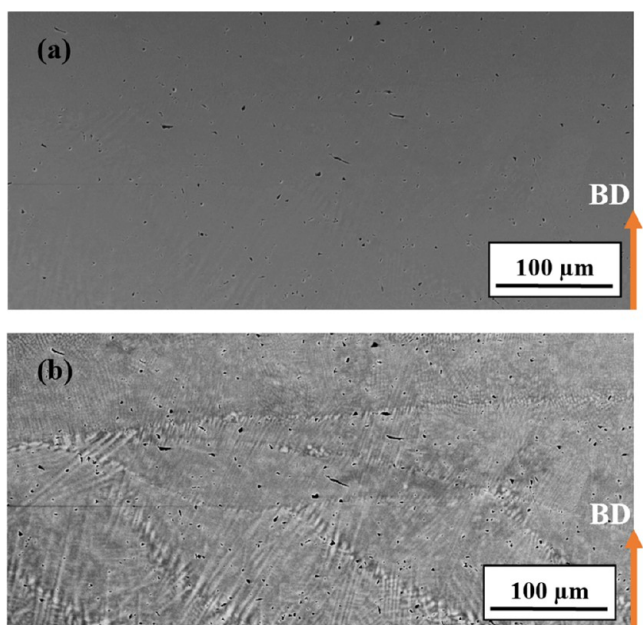

Figure 1. SEM images obtained at different modes (a-SE, b-BSE) showing the microstructure of the polished and ionic beam-treated as-manufactured TNZT-E-PBF alloy (BD cut).

defects like pores were observed. Multiple-track layers and melt pool boundaries are distinguishable in the BSE image (Figure 1b). The fusion boundary region at the top surface of the sample and multiple domains at the bottom surface of the first manufactured layer of the TNZT alloy also can be seen (Figure 1b). Minh-Son Pham et al. reported in ref 71 that the key factors in the development of the microstructure during the solidification are the speed of the liquid isotherm changes and the direction and magnitude of the thermal gradient in the liquid phase. Many studies on the solidification microstructure in the additive manufacturing of Ti−Nb-based alloys have shown that melt pool boundaries can be observed due to segregation. In particular, Guzmán et al. reported that the darker cellular walls in the BSE images of the Ti−53 wt % Nb alloy produced by L-PBF indicated the presence of the regions with a high titanium content.[72] Present observations of the darker cellular regions are due to the segregation, which is supported by the results reported in our previous study,[50] where TEM images of the as-manufactured TNZT alloy presented the α phase. In addition, the columnar dendrite structure has grown epitaxially in the successive solidification layers along the BD due to the heat flow conducted predominantly through the previously solidified layers toward the bulky stainless steel start plate.[73]

This phenomenon is similar to that in directional solidification technology, where columnar or single crystals can be accomplished with a one-dimensional cooling path.[74]

Also, as indicated by Xu et al.,[75] the molten pool boundary can strongly influence the growth of dendrites owing to its critical role in heat flow conduction.

As shown in Figure 1b, the as-manufactured TNZT alloy exhibits the presence of some dendrites, which grow normally to the molten pool boundaries, suggesting a presence of localized heat flow through molten pool boundaries.

The SE and BSE SEM images and EDS mapping of Ti, Nb, Zr, and Ta for the TNZT alloy are presented in Figure 2. A certain amount of small-size pores is visible in SEM images (Figure 2a,b), ranging from 5 to 12 μm. A small amount of unmelted and partially fused into the solid bulk powder particles is present at the bottom of the sample due to the lack of first TNZT layer fusion with the stainless steel start plate. The SEM/EDX results for the bulk TNZT alloy reveal that gray areas in the SEM-BSE image (Figure 2b) represent a matrix with uniformly distributed elements. Corresponding dark-gray areas represent Zr−Ti-rich regions and white/light
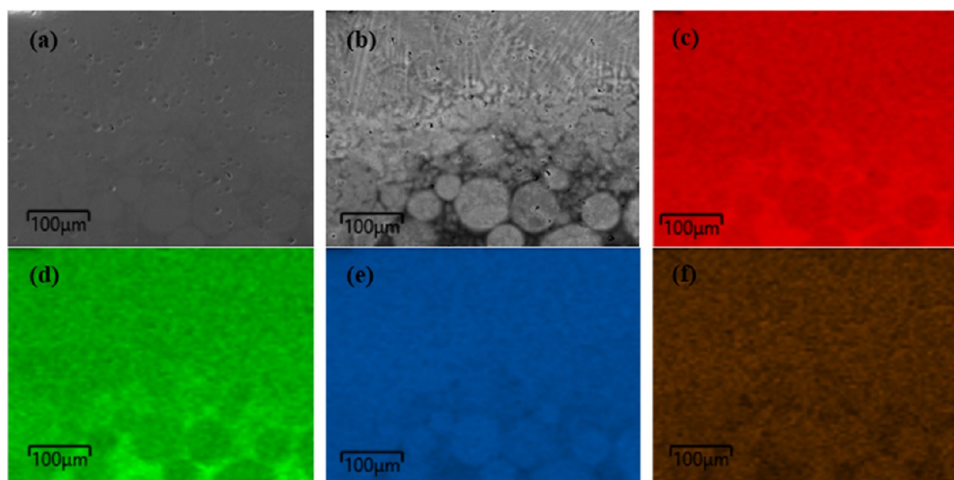

Figure 2. SE (a) and BSE (b) SEM images and EDS mapping of alloying elements Ti (c), Zr (d), Nb (e), and Ta (f) for the studied TNZT sample presented along the BD.
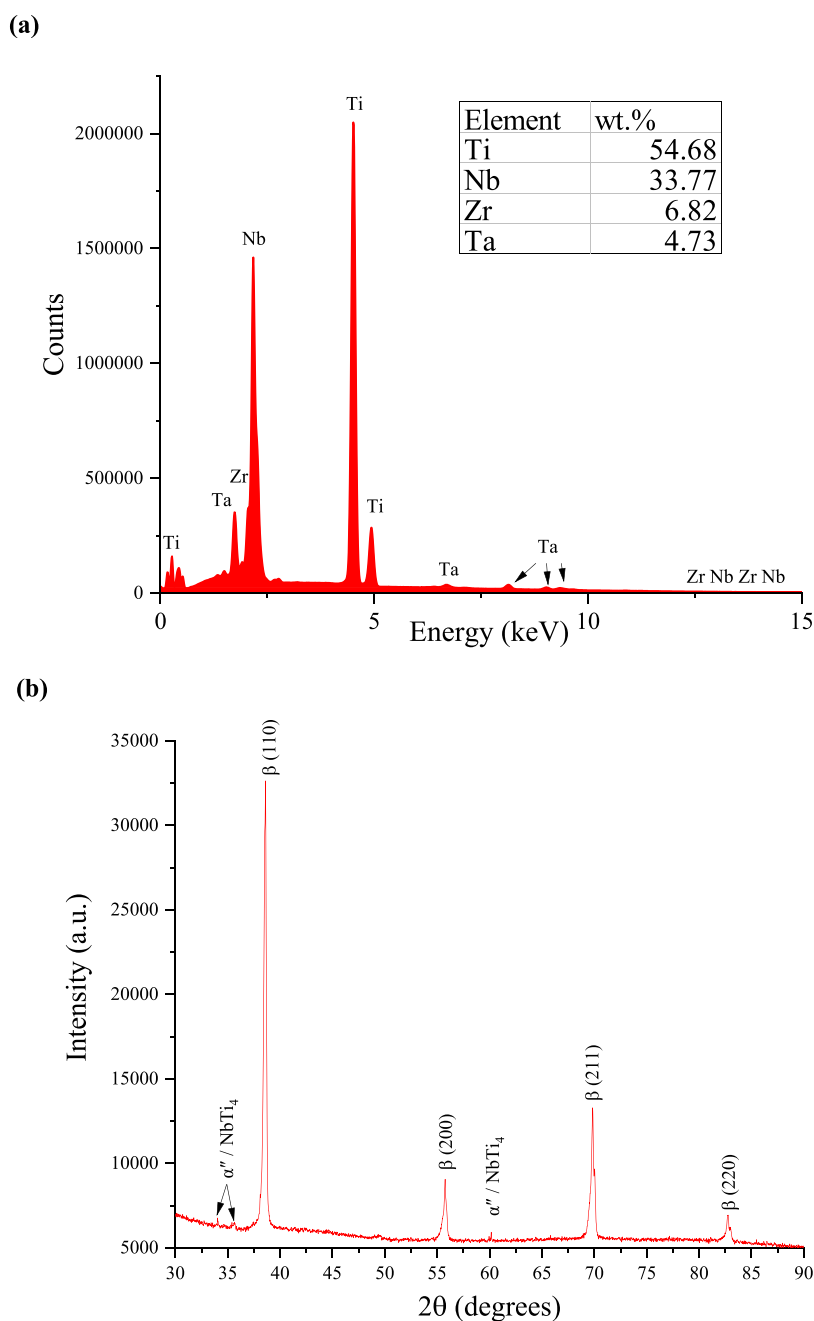
(a)

(b)

Figure 3. EDS results (a) and typical XRD profile (b) of the E-PBF manufactured TNZT alloy.

Table 1. Crystallite Size (D), Dislocation Density (δ), Microstrain (ε), and Texture (TC_{hkl}) of E-PBF Manufactured TNZT Calculated from the XRD Patterns

sample	D, nm	$\delta \cdot 10^{-3}$, nm^{-2}	$\varepsilon \cdot 10^{-3}$	TC_{200}	TC_{110}	TC_{211}	TC_{220}
E-PBF manufactured TNZT	43.20 ± 2.62	0.56 ± 0.32	1.57 ± 0.61	0.38	0.53	1.03	2.06

gray areas represent Ti-rich interdendrite regions and Ta-rich dendrite regions.

It was assumed that the regions exhibiting a dark contrast might represent partially melted zones rich in Zr and Ti owing to their lower melting point (Zr—2125 K and Ti —1941 K) compared to other elements (Ta—3017 K and Nb—2741 K). Furthermore, quantitative elemental analysis of the sample EDS spectrum reveals a good compositional homogeneity, consistent with the chemical composition of the virgin

precursor TNZT powder, with wt % contents of 54.7% for Ti, 33.8% for Nb, 6.8% for Zr, and 4.7% for Ta (Figure 3a).

The XRD patterns of the E-PBF-manufactured TNZT alloy are represented by clear (110), (200), (211), and (220) peaks (Figure 3b), which correspond to the β Ti phase (JCPDS file # 03-065-9438) with a bcc structure, with the following average lattice parameters: a = 3.2958 ± 0.0006 Å. In addition, the weak peaks at 2θ values of 34.04, 35.67, and 60.15° were detected, which can attribute to the small presence of α'' martensite and NbTi$_4$ (JCPDS file #03-065-7479) intermetal-
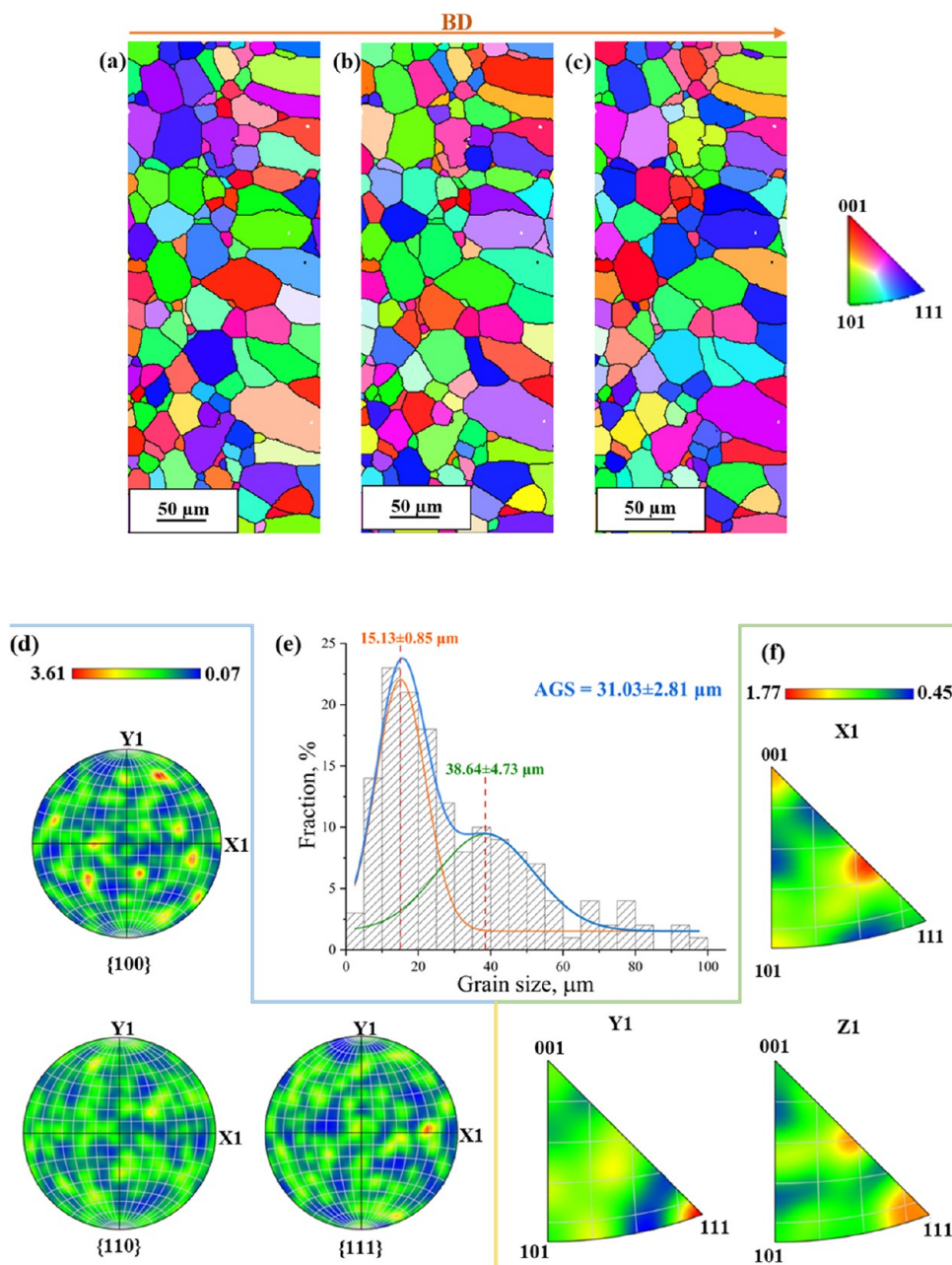
Figure 4. EBSD inverse pole figure (IPF) color maps in the x- (a), y- (b), and z-axis (c), pole figures (d) obtained from the XY plane, the bimodal grain size distribution with corresponding AGS values and the Gaussian fitting curve (e), and IPF at the scale of grain boundaries from EBSD analysis (f) for the as-built TNZT samples (cut in the BD).

lic phases in the orthorhombic crystal structure (the space group $Cmcm$).[76,77] It is in good agreement with our previously reported results in ref 50 of the TEM study of the as-manufactured TNZT alloy, which have shown the presence of the equiaxed β-grains with the fine dispersion of nanocrystalline α'' and $NbTi_4$ phases together with β-Ti twins.

Corresponding parameters of as-manufactured TNZT samples extracted from the XRD spectra are presented in Table 1. The texture coefficients for all detected bcc planes (TC_{hkl}) were used for the determination of the quantitative data concerning the preferential crystallite orientation based on the approach described in ref 78. The higher value of the texture coefficient ($TC_{hkl} > 1$) represents the abundance of grain, which is formed in a given [hkl] direction. The value $0 <$ $TC_{hkl} < 1$ indicates a decrease in atom density along a particular crystal plane as compared to the reference data.

In addition, based on the obtained data, it is shown that the surface texture of the samples along the BD is redistributed and reveals the preferential lattice structure orientation in the (211) and (220) crystal planes (Table 1).

This can be due to the influence of the processing parameters of E-PBF on texture evolution. Nevertheless, the as-manufactured samples still have a maximum XRD peak intensity at $2\theta = 38.59°$, which corresponds to the (110) plane of the β phase. It was also found that the calculated crystallite size,[79] dislocation density,[80,81] and microstrain[82] were the same as we obtained in our previous work (Table 1).[50]

EBSD analysis (Figure 4) was performed for the cut along the BD in order to further highlight the grain morphology of

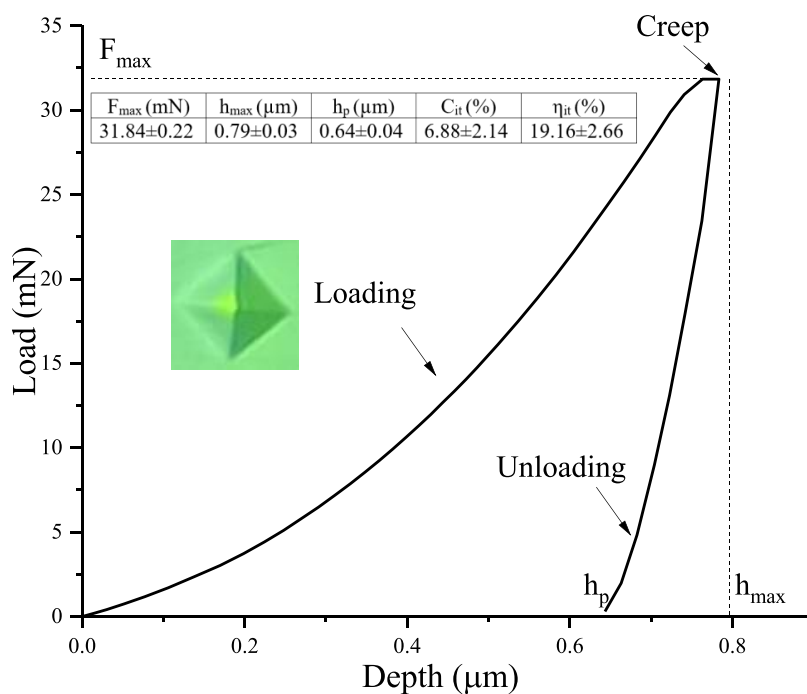| F_{max} (mN)	h_{max} (µm)	h_p (µm)	C_{it} (%)	η_{it} (%)
31.84±0.22	0.79±0.03	0.64±0.04	6.88±2.14	19.16±2.66

Figure 5. Nanoindentation results of typical load−depth relationships obtained for TNZT.

the studied samples. Figure 4a−c shows the IPF maps, which are almost entirely composed of the patterns corresponding to the β Ti bcc phase grains (86.6%). The low content of other phase or phases was detected (13.4%), which, based on our XRD results, can be attributed to α''-Ti (martensitic structure). Similar results were reported by Rossi et al.[77] It was revealed that the β phase (90%) is a predominant phase in the TNZT alloy. However, a small amount of α''-Ti content with short needle-like shape grains was also located on the β-Ti grain boundaries. According to the EBSD analyses (Figure 4a−c), the random texture and predominantly random orientation distribution of grains were observed for all axes, which means that there is no preferential crystallographic orientation of the grains. Thus, there is no imposed anisotropy on these samples due to their grain orientation. This fact may indicate that the macroscopic mechanical properties of the samples should be isotropic. However, it is important to note that while the absence of a preferential crystallographic orientation suggests isotropic behavior, it does not guarantee complete isotropy in all mechanical properties. Other microstructural features or external factors can still influence the mechanical behavior of the material.

The TNZT alloy consists of β grains with different morphologies (elongated and fine equiaxed grains) depending on their location (Figure 4a−c). Indeed, elongated β grains, which have an inclination of approximately 30° with respect to the BD, can mainly be found along the melt pool of the top layer. In contrast, at the bottom of the layer, there are mainly smaller equiaxed β grains. The grain size was calculated as an equivalent circle diameter using the grain area from the distributions (Figure 4e). It was revealed that the bimodal grain size microstructure showed a dominance of grains with a size of less than 40 µm, with twice the frequency compared to larger grains. According to the Gaussian fitting method, the bimodal grain size distribution exhibited two distinct peaks at 15.13 ± 0.85 and 38.64 ± 4.73 µm. In addition, the average grain size (AGS) for the studied TNZT samples was

determined to be 31.03 ± 2.81 µm. A weak crystallographic texture with maximum texture intensity of 3.61 was denoted by the pole figures obtained from the XY plane along the BD of the as-fabricated samples (Figure 4d). Along with this relatively small number of grains with a (100) orientation was detected. In addition, IPFs indicated a weak texture with maximum texture indices of 1.77 (Figure 4f).

The absence of a dominant direction for the grain lattice orientation could be due to the high alloy element content and long *in situ* high-temperature heat treatment of the lower manufactured layers resulting from the high beam energy applied in the current top layer processed.

The hardness (H_N) and Young's modulus (E_N) were measured for the cross section of the TNZT alloy samples after the ionic beam treatment using the nanoindentation with a load and holding time of 30 mN and 10 s, respectively. One of the targets was studying the influence of the microstructure on mechanical properties. The average measured H_N, E_N, and maximum penetration depth evaluated for the sample cuts along the BD were 2.01 ± 0.22, 69.48 ± 0.03, and 0.76 ± 0.03 µm, respectively. It was observed that the microstructure and mechanical properties of the additively manufactured E-PBF TNZT samples are quite homogeneous. Although the studied depth of the surface layer does not exceed 3500 µm (see Figure S1 in the Supporting Information).

In addition, we conducted a detailed study of the load−depth relations of the E-PBF-TNZT samples. It was revealed that the trend of the curves is the same along the BD (see Figure S2 in the Supporting Information). Figure 5 shows a typical load−depth curve for studied samples along with the important collected indentation parameters and a typical nanoindentation imprint.

It is evident that the load−depth curve is continuous, without any large steps (pop-ins or pop-outs). Based on ref 83, we calculated the corresponding elastic recovery ratio (19.35%) and the value of characteristic plasticity (80.65%), which are consistent with the collected data of the elastic part
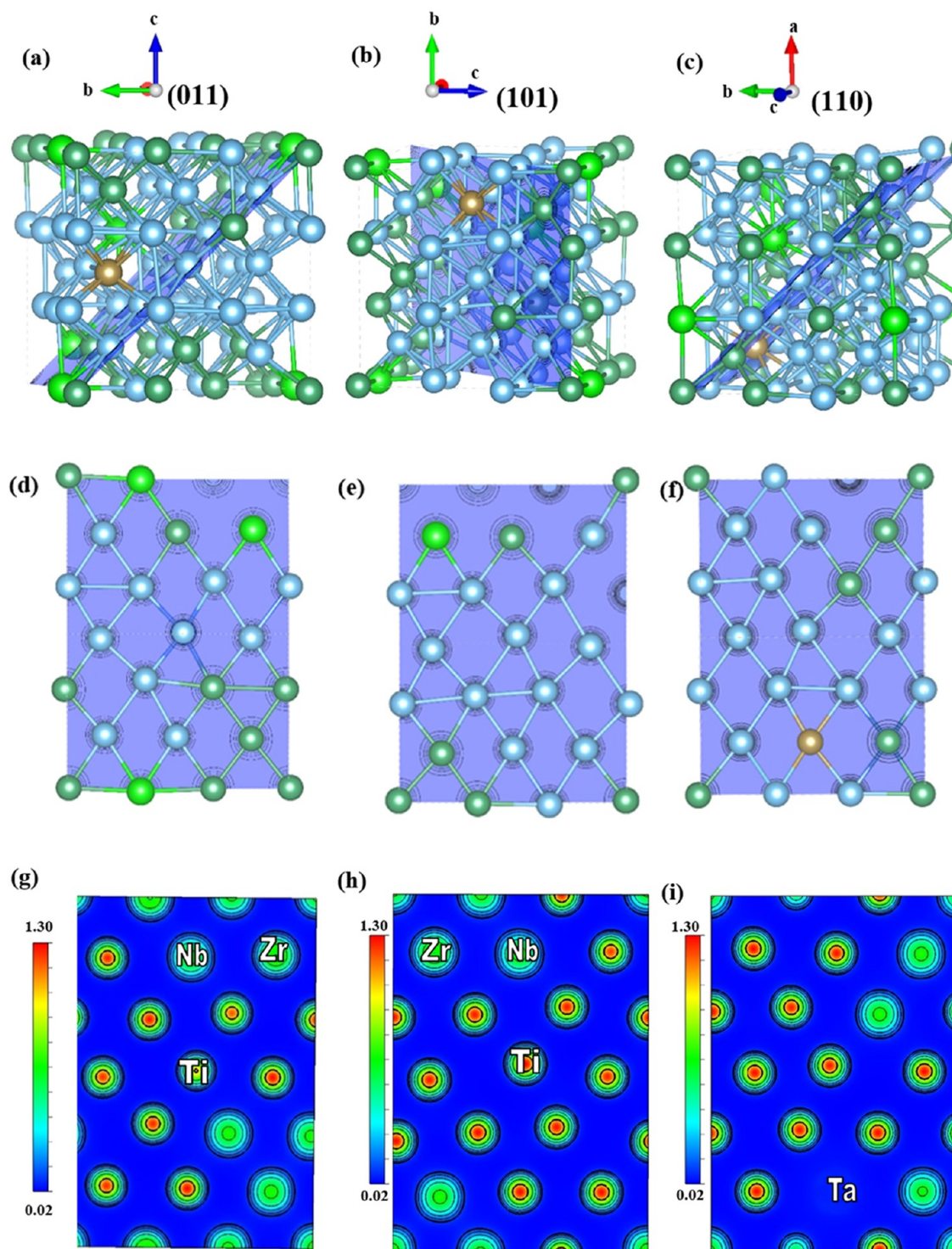
Figure 6. Atomic configuration of the TNZT alloys in a 3 × 3 × 3 supercell (54 atoms) after geometry relaxation (a–c), the projection of the TNZT structure to the (011) (d), (101) (e), and (110) (f) planes, and the charge density distribution in the (011) (g), (101) (h), and (110) (i) planes. Small blue, green, light green, and brown spheres are Ti, Nb, Zr, and Ta atoms, respectively.

of indentation work (19.16%) and detected the domination of plastic deformation. Moreover, no cracks are observed in the typical nanoindentation imprint, indicating the plastic behavior of TNZT. Furthermore, the edges of the imprint are quite clear, without any bulging along the indentation edges.

The first-principles DFT calculations were performed to study the stability and mechanical characteristics of the multicomponent TNZT alloy for a better understanding of

the nature of its low elasticity and to predict the mechanical properties based on the calculated DFT results. The lattice parameter (a_{DFT}), density (ρ), E_f, E_{coh}, H_{DFT}, and elastic constants of the TNZT alloy are calculated. The ductile/brittle properties of the TNZT alloys are analyzed based on the mechanical characteristic of the shear modulus-to-bulk modulus (G/B) ratio, Poisson's ratio (ν), and Cauchy pressure (C'). The evaluated thermodynamic properties of the TNZT

Table 2. Calculated Values for the Elastic Constants $\overline{C}_{11}$ (GPa), $\overline{C}_{12}$ (GPa), and $\overline{C}_{44}$ (GPa), E_f (meV/atom), E_{coh} (eV/atom), Bulk Modulus (B in GPa), Shear Modulus (G in GPa), Young's Modulus (E in GPa), G/B Ratio, Poisson's Ratio (ν), Cauchy Pressure (C' in GPa), Anisotropic Ratio of Zener (A), Melting Point (T_m in K), Hardness (H in GPa), Debye Temperature (θ_D in K), Shear Sound Velocity (v_s in g·s^{-1}), Longitudinal Sound Velocity (v_l in g·s^{-1}), Average Wave Velocity (v_m in g·s^{-1}), Molar Mass (M in g/mol), and Minimal Thermal Conductivity (k_{min} in W·(m·K)$^{-1}$) of the bcc Ti−13Nb−3Zr−Ta Structure

composition	$\overline{C}_{11}$	$\overline{C}_{12}$	$\overline{C}_{44}$	E	A	ν	B	G	G/B	C'
Ti−13Nb−3Zr−Ta (54 atoms)	121.84	100.23	23.84	49.40	2.21	0.42	107.43	17.35	0.162	98.00
	k_{min}	E_f	E_{coh}	T_m	H_{DFT}	θ_D	v_s	v_l	v_m	M
	4.03	−15.55	−5.73	2129	1.87	164	1713.24	4699.81	1945.59	34.35

alloy were represented by the melting point temperature and Debye temperature. In addition, the metallicity and anisotropy of the TNZT alloy were also estimated. The character of chemical bonding of the studied alloy was represented by analyzing the electron structure CDD, Bader charge, and ELF.

First, the position of atoms in the supercell and crystal configurations of the TNZT alloy were optimized, and these relaxed atomic configurations (a local minimum) were chosen for further study. The optimized structure of the four-component alloy, which we used here for further detailed analysis, is shown in Figure 6a−c.

As shown in Figure 6, the TNZT alloy retains the bcc lattice structure during the relaxation of the atomic positions. It is known that in most cases, the microstructure of the multicomponent alloys is not homogeneous, revealing a nonuniform interatomic spacing distribution (Figure 6d−f). This is due to preferential interactions between atoms of different types.[84]

Figure 6g−i shows the charge density distribution in the (011), (101), and (110) planes. It is clear that in the TNZT supercell, the electronic charge is almost entirely localized at the Ti sites with the maximum electronic charge density of 1.3 $\overline{e}$/Bohr^3. The electronic charge density of Nb, Zr, and Ta atoms is equal to 0.7, 0.7, and 0.06 $\overline{e}$/Bohr^3, respectively (Figure 6g−i).

The lattice parameter and density of the bcc TNZT structure are calculated to be a_{DFT} = 3.2930 Å and ρ = 5.911 g/cm^3, respectively. These results are in good agreement with our XRD results and other theoretical and experimental data,[85] which points to a good accuracy of obtained results.

In order to evaluate the structural stability of the TNZT alloy, E_f and E_{coh} are calculated (Table 2). Based on the definition of E$_\beta$ a negative value means that the alloying ability of the elements is strong. In the case of cohesion evaluation, the higher absolute value of the E_{coh} indicates a more stable structure.[86] The calculated E_{coh} (−5.73 eV/atom) of the studied TNZT structure is consistent with other theoretically acquired values (−6.70 eV/atom)[87] and indirectly reflects that it has the rather stable TNZT bcc structure. Therefore, it is possible to conclude that Nb, Zr, and Ta indeed act as β-phase stabilizers. In addition, the constructed TNZT supercell has a negative E_f (−15.50 meV/atom), pointing to a good alloying ability, which confirms that there is a strong chemical interaction between the Zr, Ti, Ta, and Nb atoms. Based on the obtained results, it can be concluded that the presence of a small amount of martensite phase in the β matrix of the TNZT alloy observed by XRD is attributed to the intense localized heating caused by the electron beam and the subsequent rapid cooling, rather than the design of the alloy composition.

The elastic constants are commonly used for the evaluation of the material's ability to resist the deformation inflicted by external forces. And they play a key role in estimating the anisotropic behavior and structural stability of materials. The corresponding elastic constants of the TNZT alloy were calculated by VASP (Table 2). Obtained results are in good agreement with the experimental and theoretical values reported in other studies,[17,87,88] and correspond to other multicomponent alloys based on β Ti with a similar composition, which indicates that calculated results are credible.

A widely used mechanical stability criterion for elastic constants in the bcc structure was proposed by Born et al.:[89] $\overline{C}_{11}−|\overline{C}_{12}| > 0$; $\overline{C}_{11} + 2\overline{C}_{12} > 0$; $\overline{C}_{44} > 0$. The obtained elastic constants of TNZT alloys satisfy these stability criteria, revealing that the structures of the TNZT alloys should be mechanically stable.

The mechanical properties of the TNZT alloys were further analyzed by the evaluation of the bulk modulus, the shear modulus, Young's modulus, Poisson's ratio, the Cauchy pressure, and the anisotropy coefficient based on the calculated single-crystal elastic constants using Voigt−Reuss−Hill approximations (Table 2).

It is known that the G/B ratio can be used for better understanding the brittle and ductile behavior of the alloys, with the high G/B values indicating good ductility (corresponding critical G/B value is about 0.57). Obtained results revealed that all G/B values of the TNZT alloys are less than 0.57 (Table 2), which means that the alloy should be ductile. In addition, the Cauchy pressure can be used for the characterization of the bonding type (covalent or metallic) between the atoms.[90] A positive (negative) Cauchy pressure value of the material indicates a metallic (covalent) character of the bonding mechanism of a ductile (brittle) nature. Ductility and plasticity are well-established concepts in materials science, which, although related, exhibit distinct characteristics. While high plasticity is a prerequisite for high ductility, it does not guarantee it. Therefore, directly comparing our DFT results with experimental data regarding the ductile and plastic behavior of the TNZT alloy is not feasible. Nevertheless, the simulated data does indicate the presence of ductile behavior in TNZT, which aligns with previous studies reporting an excellent combination of relatively low elasticity and significant ductility in the TNZT alloy.[91] Moreover, in general, the β-phase of titanium is known to exhibit higher ductility compared to other titanium phases, primarily due to the larger number of slip planes present in its bcc structure. Based on the preceding discussion and the aforementioned findings, it can be concluded that the E-PBF-fabricated TNZT alloy is expected to possess a large ductility.

Corresponding calculated Cauchy pressures for the TNZT alloy are positive, revealing the dominant role of the metallic bonding and indicating good ductility, which is consistent with
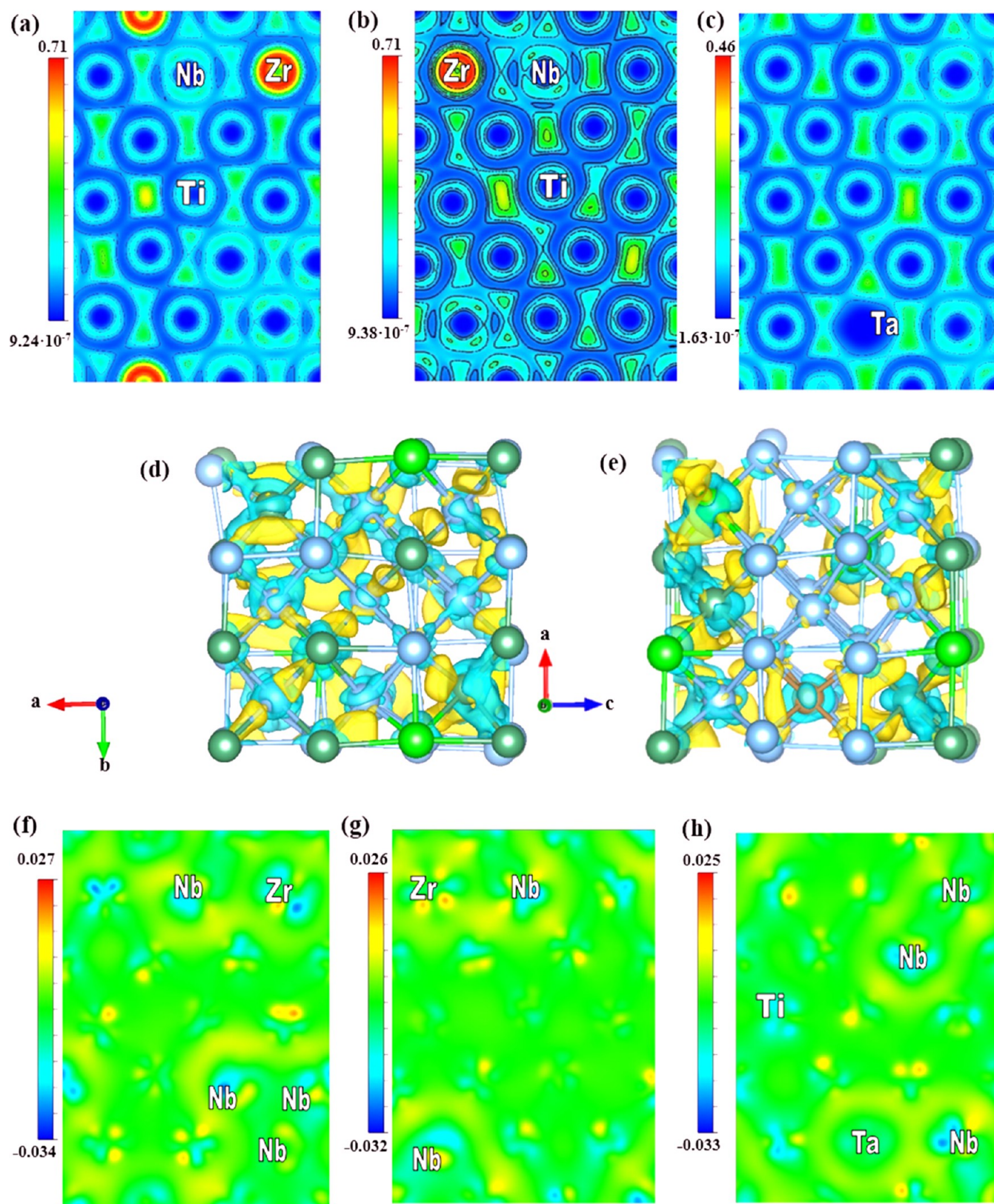
Figure 7. Contour plots of ELF on the (011) (a), (101) (b), and (110) (c) planes, 3D views of interfacial CDD (d, e), and the (011) (f), (101) (g) and (110) (h) plane views of CDD. The isosurface of CDD is 0.008 e·Å^{-3}. Relative electron density and ELF values are color-coded (corresponding bars to the left of the images). Red-yellow and blue regions refer to electron depletion and accumulation, respectively.

the value of the G/B ratio. Furthermore, Poisson's ratio was above 0.29 (see Table 2), which also reflects that the bonds in the material are metallic in nature.

The melting point (T_m) is known to be a rather important parameter in the design of new promising materials, and its prior knowledge is of high importance, for example, when
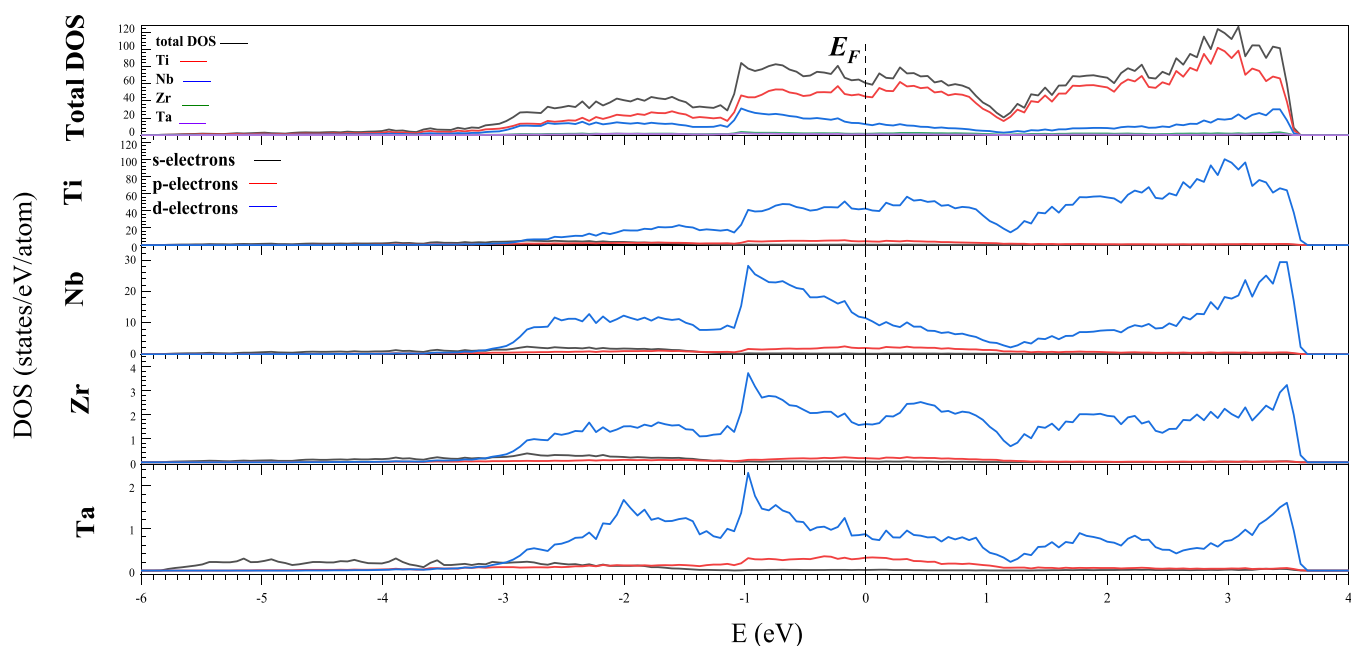
Figure 8. Calculated total and partial DOS for TNZT. The dashed line denotes E_F.

designing process parameters for additive manufacturing of new materials. Experimental evaluation of such parameters for a single alloy is relatively straightforward, but screening such parameters for a range of different materials can be a serious undertaking. Thus, theoretically, predicting such parameters for previously untested alloys have a serious value. The corresponding melting point for TNZT was calculated to be equal to 2129 K. This value is reasonably close to the experimental value for the Ti−45Nb atom % alloy (1900 K), which shows that our calculation results are credible.

The calculated Young's modulus is also presented in Table 2. It can be seen that the calculated modulus is lower than the measured one. One can suggest that the reason for this could be that our first-principles calculation was limited to bulk single crystals and did not take into account various factors such as the presence of pores and other defects, the specifics of the layered structure, and other parameters and effects associated with additive manufacturing. Nevertheless, the value of the calculated Young's modulus is rather close to the experimentally measured one.

The degree of anisotropy can be characterized by the anisotropy factor A. The material belongs to an isotropic crystal if $A = 1$ and is anisotropic when the A value deviates from 1. The higher the deviation of A, the larger anisotropy the material has.

Calculated results presented in Table 2 reveal that the anisotropic factors of the TNZT alloy are higher than 1, which means that the material is anisotropic. Moreover, this anisotropic character was confirmed by Young's modulus values calculated for (100), (110), and (111) directions equal to 31, 60, and 67 GPa, respectively. Tane et al.[92] reported that Young's modulus of single TNTZ crystals with the bcc structure shows the same θ-dependent anisotropy as obtained in present studies. Thus, based on these results and our experimentally observed data, we can conclude that the used alloying elements can significantly improve the mechanical properties of the Ti-based alloy manufactured by E-PBF.

Material hardness plays a key role in the field of materials engineering, particularly in evaluating the wear behavior of materials. Thus, it is very important to evaluate the hardness of manufactured materials. It can be calculated by using Poisson's ratio and Young's modulus as follows[93]

$$H_{DFT} = \frac{(1 - 2\nu)E_{DFT}}{6(1 + \nu)} \tag{1}$$

The calculated result of hardness is presented in Table 2. The obtained hardness value closely aligns with the experimental values, indicating the credibility of our DFT results and the feasibility of using the DFT calculations for predicting mechanical properties.

The Debye temperature (θ_D), which is directly related to the atomic thermal vibration, is an important fundamental physical quantity of solids. It reflects the degree of dynamic distortion of the crystal lattice and characterizes the binding force between atoms. The Debye temperature is closely related to a wide range of physical properties of solids, such as lattice stability, acoustic velocity, specific heat capacity, and thermal expansion coefficient. In order to further understand the thermodynamic behavior and lattice stability of the TNZT alloys, it was necessary to calculate the θ_D values and determine its variation rule, which is very important for the design and development of these alloys. According to the obtained B and G values, we determined the ν_s, ν_l, and ν_m and further studied the θ_D and k_{min}. Corresponding values are also listed in Table 2. The θ_D and k_{min} are determined to be 164 K and 4.03 W·$(m·K)^{-1}$, respectively. However, as far as we know, there are no published data available for comparison.

To further explore the character of the chemical bonding of TNZT alloys, we also calculated ELF, which can indicate the bond origin and gives a quantitative picture of the chemical bonding mechanism. Figure 7 illustrates the ELF of Ti, Nb, Zr, and Ta atoms on the (011), (101), and (110) planes of the TNZT supercell. In the color map, dark blue (ELF ≈ 0.) indicates the maximum delocalization, and red (ELF = 0.71) represents the maximum localization of electrons. Although the

core region of Zr atoms is much higher (ELF = 0.71) (Figure 7a,b) than other atoms, the ELF value around the Zr atoms is not highly localized (0.1 < ELF < 0.26), which indicates a mixture of metallic bonds with a slight covalent component between Zr and Nb atoms and metallic bonds between Zr and Ti atoms.

The ELF values of the Ta atom are close to zero, which means that the electrons around the Ta atom are in a highly delocalized state. However, there is an electron gas with an ELF value of ~0.32 between Ti and Ta atoms, which indicates that Ti−Ta bonding can be a mixture of covalent bonds and metallic bonds. The ELF values for Nb−Nb, Ti−Ti, and Nb−Ti atoms are in the range of 0.23 to 0.38, which reveals the mixture of slight covalent bonding character with almost pure metallic bonding.

The CDD of electronic charge was calculated to further understand the origin of the atomic bonding based on charge accumulation and depletion (Figure 7d−h). It is clear that the electrons shifted from Ti atoms to the neighboring Nb, Zr, and Ta atoms forming a strong covalent Ti−Nb bond and weak covalent Ti−Zr and Ti−Ta bonds. Also, the Zr atoms donate electrons to the neighboring Nb ones, making Nb more negatively charged and revealing the weak covalent bonds between the atoms (Figure 7b,e). In addition, there is an indication that some homopolar covalent Ti−Ti and Nb−Nb bonds are formed as well. Clearly, metallic Ti−Ti and Nb−Nb bonds were also identified. It has to be mentioned that the CDD method indicates that TNZT has only bonds with the first neighbors between Ti and added Nb, Zr, and Ta atoms.

Bader analysis also shows that Ti and Zr atoms lost 11.84 and 0.72 e, respectively. Most part of the charge transfer from Ti and Zr atoms corresponds to the Nb atoms (10.96 e). A Ta atom gains about 1.60 valence electrons from surrounding Ti atoms. It is clear that Nb attracts a higher amount of valence electrons, which leads to the formation of a dominantly covalent Ti−Nb bonding.

The fundamental aspects regarding the chemical bonding mechanisms responsible for stabilizing the β-phase in Ti alloys through alloying remain largely unresolved. However, insights into this phenomenon can be gained by examining the electronic DOS, which provides information on the occupation of energy levels (i.e., the number of electronic states per unit of energy).

By analyzing the DOS occupation and the position of the pseudogap, usually formed by d-elements in alloys, relative to the Fermi level (E_F), it becomes possible to predict the nature of chemical bonding, whether it is predominantly metallic or covalent.

Figure 8 illustrates the DOS for TNZT, with energy levels ranging from −5.8 to 3.6 eV. The vertical dashed line represents the E_F, denoted as the zero-energy point (see Figure S3 in the Supporting Information). The corresponding partial DOS curves reveal that all atoms make nearly equal contributions to the total DOS within the pseudogap region, with Ti exhibiting the highest value at the E_F. The significant DOS value at E_F, situated within the bonding region, signifies the presence of metallic bonding between atoms.

Thus, the calculated results revealed that low C' and $\overline{C}_{44}$ lead to a lowered Young's modulus, and therefore, it could indicate that the softening in C' and $\overline{C}_{44}$ is the origin of the low elasticity of TNZT. Moreover, based on our DFT analysis, we conclude that the observed softening phenomenon of C' and $\overline{C}_{44}$ is related to the weakness of the second and third neighbor

bonds in comparison with first neighbor bonds. This also explains why $E_{(100)}$ is lower than $E_{(110)}$ and $E_{(111)}$.

■ CONCLUSIONS

In this paper, a combined first-principles DFT calculations and experimental study on the microstructure, structural stability, thermal characteristics, mechanical properties, and electronic structure of the multicomponent TNZT alloy is presented, aiming to explore the nature of its low elasticity, which is of high interest for the development of new promising β-stabilized Ti-based alloys for biomedical applications.

The main conclusions of this study are as follows:

- The studied β TNZT alloy manufactured by E-PBF exhibits homogeneous mechanical properties along the BD, which are dictated by the crystallographic texture and microstructure morphologies.
- The presence of a small amount of α'' martensite phase within the β matrix of the TNZT alloy is attributed to intense localized heating induced by the electron beam and the subsequent rapid cooling rather than the specific alloy composition design.
- TNZT has a mixture of strong metallic and weak covalent bonding.
- The softening in the Cauchy pressure (C') and elastic constant $\overline{C}_{44}$ is the origin of the low elasticity of TNZT.
- The nature of this softening phenomenon of C' and $\overline{C}_{44}$ can be related to the weakness of the second and third neighbor bonds in comparison with the first neighbor bonds in TNZT.
- A carefully designed TNZT alloy can be an excellent candidate for the manufacturing of orthopedic internal fixation devices.

■ ASSOCIATED CONTENT

ⓈⒾ Supporting Information

The Supporting Information is available free of charge at https://pubs.acs.org/doi/10.1021/acsomega.3c03157.

Hardness and Young's modulus distribution along the BD, Figure S1; load−depth relationships, Figure S2; and total and partial DOS, Figure S3 (PDF)

■ AUTHOR INFORMATION

Corresponding Author

Irina Yu. Grubova − *Physical Materials Science and Composite Materials Centre, Research School of Chemistry & Applied Biomedical Sciences, National Research Tomsk Polytechnic University, Tomsk 634050, Russia;* ⓞ orcid.org/0000-0003-3632-0754; Phone: +79131104676; Email: rodeo_88@mail.ru

Authors

Roman A. Surmenev − *Physical Materials Science and Composite Materials Centre, Research School of Chemistry & Applied Biomedical Sciences, National Research Tomsk Polytechnic University, Tomsk 634050, Russia;* ⓞ orcid.org/0000-0002-8061-3047

Erik C. Neyts − *Department of Chemistry, PLASMANT Research Group, NANOlab Center of Excellence, University of Antwerp, B-2610 Antwerp, Belgium;* ⓞ orcid.org/0000-0002-3360-3196

Andrey V. Koptyug − *Sports Tech Research Centre, Mid Sweden University, SE-831 25 Östersund, Sweden*

Anastasia P. Volkova − *Physical Materials Science and Composite Materials Centre, Research School of Chemistry & Applied Biomedical Sciences, National Research Tomsk Polytechnic University, Tomsk 634050, Russia*

Maria A. Surmeneva − *Physical Materials Science and Composite Materials Centre, Research School of Chemistry & Applied Biomedical Sciences, National Research Tomsk Polytechnic University, Tomsk 634050, Russia*

Complete contact information is available at:
https://pubs.acs.org/10.1021/acsomega.3c03157

Notes

The authors declare no competing financial interest.

◼ REFERENCES

(1) Rao, S.; Ushida, T.; Tateishi, T.; Okazaki, Y.; Asao, S. Effect of Ti, Al, and V Ions on the Relative Growth Rate of Fibroblasts (L929) and Osteoblasts (MC3T3-E1) Cells. *Bio-Med. Mater. Eng.* **1996**, *6*, 79−86.

(2) Walker, P. R.; LeBlanc, J.; Sikorska, M. Effects of Aluminum and other Cations on the Structure of Brain and Liver Chromatin. *Biochemistry* **1989**, *28*, 3911−3915.

(3) Ho, W. F.; Ju, C. P.; Lin, J. C. Structure and Properties of Cast Binary Ti−Mo Alloys. *Biomaterials* **1999**, *20*, 2115−2122.

(4) Kolli, R. P.; Devaraj, A. A Review of Metastable Beta Titanium Alloys. *Metals* **2018**, *8*, 506.

(5) Davoodi, E.; Montazerian, H.; Mirhakimi, A. S.; Zhianmanesh, M.; Ibhadode, O.; Shahabad, S. I.; Esmaeilizadeh, R.; Sarikhani, E.; Toorandaz, S.; Sarabi, S. A.; Nasiri, R.; Zhu, Y.; Kadkhodapour, J.; Li, B.; Khademhosseini, A.; Toyserkani, E. Additively Manufactured Metallic Biomaterials. *Bioact. Mater.* **2022**, *15*, 214−249.

(6) Konopatsky, A. S.; Dubinskiy, S. M.; Zhukova, Y. S.; Sheremetyev, V.; Brailovski, V.; Prokoshkin, S. D.; Filonov, M. R. Ternary Ti-Zr-Nb and Quaternary Ti-Zr-Nb-Ta Shape Memory Alloys for Biomedical Applications: Structural Features and Cyclic Mechanical Properties. *Mater. Sci. Eng. A* **2017**, *702*, 301−311.

(7) Geetha, M.; Singh, A. K.; Muraleedharan, K.; Gogia, A. K.; Asokamani, R. Effect of Thermomechanical Processing on Microstructure of a Ti−13Nb−13Zr Alloy. *J. Alloys Compd.* **2001**, *329*, 264−271.

(8) Tang, X.; Ahmed, T.; Rack, H. J. Phase Transformations in Ti-Nb-Ta and Ti-Nb-Ta-Zr Alloys. *J. Mater. Sci.* **2000**, *35*, 1805−1811.

(9) Cordeiro, J. M.; Barão, V. A. Is there scientific evidence favoring the substitution of commercially pure titanium with titanium alloys for the manufacture of dental implants? *Mater. Sci. Eng.* **2017**, *71*, 1201−1215.

(10) Liu, Q.; Meng, Q.; Guo, S.; Zhao, X. α′Type Ti−Nb−Zr alloys with ultra-low Young's modulus and high strength. *Prog. Nat. Sci.: Mater. Int.* **2013**, *23*, 562−565.

(11) Correa, D. R. N.; Vicente, F. B.; Donato, T. A. G.; Arana-Chavez, V. E.; Buzalaf, M. A. R.; Grandini, C. R. The effect of the solute on the structure, selected mechanical properties, and biocompatibility of Ti−Zr system alloys for dental applications. *Mater. Sci. Eng. C* **2014**, *34*, 354−359.

(12) Inaekyan, K.; Brailovski, V.; Prokoshkin, S.; Pushin, V.; Dubinskiy, S.; Sheremetyev, V. Comparative Study of Structure Formation and Mechanical Behavior of Age-Hardened Ti−Nb−Zr and Ti−Nb−Ta Shape Memory Alloys. *Mater. Charact.* **2015**, *103*, 65−74.

(13) Wang, J.; Li, Q.; Xiong, C.; Li, Y.; Sun, B. Effect of Zr on the Martensitic Transformation and the Shape Memory Effect in Ti−Zr−Nb- Ta High-Temperature Shape Memory Alloys. *J. Alloys Compd.* **2018**, *737*, 672−677.

(14) Salvador, C. A. F.; Lopes, E. S. N.; Ospina, C. A.; Caram, R. Orthorhombic Martensite Formation Upon Aging in a Ti-30Nb-4Sn Alloy. *Mater. Chem. Phys.* **2016**, *183*, 238−246.

(15) Fanton, L.; de Lima, N. B.; de Oliveira França Hayama, A.; Caram, R.; Fogagnolo, J. B. Texture Development in Cold Deformed and Recrystallized Ti−30Nb−4Sn Alloy and Its Effects on Hardness and Young's Modulus. *Adv. Eng. Mater.* **2017**, *19*, No. 1600058.

(16) Wang, J. C.; Liu, Y. J.; Qin, P.; Liang, S. X.; Sercombe, T. B.; Zhang, L. C. Selective Laser Melting of Ti-35Nb Composite From Elemental Powder Mixture: Microstructure, Mechanical Behavior and Corrosion Behavior. *Mater. Sci. Eng. A* **2019**, *760*, 214−224.

(17) Karre, R.; Niranjan, M. K.; Dey, S. R. First Principles Theoretical Investigations of Low Young's Modulus Beta Ti−Nb and Ti−Nb−Zr Alloys Compositions for Biomedical Applications. *Mater. Sci. Eng. C* **2015**, *50*, 52−58.

(18) Veríssimo, N. C.; Figueiredo, R. S.; de Oliveira, H. G.; Rodrigues, C. A.; Caram, R.; Bertazzoli, R. Characterization of the Photoactivity of Nanotube Layers Grown on Ti−35Nb and Ti−35Nb−4Sn Alloys. *J. Mater. Sci.* **2016**, *51*, 9384−9393.

(19) Santos, D. R.; Pereira, M. D. S.; Cairo, C. A. A.; Graca, M. L. A.; Henriques, V. A. R. Isochronal Sintering of the Blended Elemental Ti−35Nb Alloy. *Mater. Sci. Eng. A* **2008**, *472*, 193−197.

(20) Babilas, D.; Urba′ nczyk, E.; Sowa, M.; Maciej, A.; Korotin, D. M.; Zhidkov, I. S.; Basiaga, M.; Krok-Borkowicz, M.; Szyk-Warszynska, L.; Pamuła, E.; et al. On the Electropolishing and Anodic Oxidation of Ti-15Mo Alloy. *Electrochim. Acta* **2016**, *205*, 256−265.

(21) Nag, S.; Banerjee, R.; Fraser, H. L. Microstructural Evolution and Strengthening Mechanisms in Ti−Nb−Zr−Ta, Ti−Mo−Zr−Fe and Ti−15Mo Biocompatible Alloys. *Mater. Sci. Eng. C* **2005**, *25*, 357−362.

(22) Banerjee, S.; Naik, U. M. Plastic Instability in an Omega Forming Ti-15% Mo Alloy. *Acta Mater.* **1996**, *44*, 3667−3677.

(23) Nag, S.; Banerjee, R.; Stechschulte, J.; Fraser, H. L. Comparison of Microstructural Evolution in Ti-Mo-Zr-Fe and Ti-15Mo Biocompatible Alloys. *J. Mater. Sci. Mater. Med.* **2005**, *16*, 679−685.

(24) Hussein, A. H.; Gepreel, M. A. H.; Gouda, M. K.; Hefnawy, A. M.; Kandil, S. H. Biocompatibility of New Ti−Nb−Ta Base Alloys. *Mater. Sci. Eng. C* **2016**, *61*, 574−578.

(25) Liu, Y. J.; Li, X. P.; Zhang, L. C.; Sercombe, T. B. Processing and Properties of Topologically Optimised Biomedical Ti−24Nb−4Zr−8Sn Scaffolds Manufactured by Selective Laser Melting. *Mater. Sci. Eng. A* **2015**, *642*, 268−278.

(26) Zhang, L. C.; Sercombe, T. B. Selective Laser Melting of Low-Modulus Biomedical Ti-24Nb-4Zr-8Sn Alloy: Effect of Laser Point Distance. *Key Eng. Mater.* **2012**, *520*, 226−233.

(27) Liu, Y.; Li, S.; Hou, W.; Wang, S.; Hao, Y.; Yang, R.; Sercombe, T. B.; Zhang, L.-C. Electron Beam Melted Beta-Type Ti−24Nb−4Zr−8Sn Porous Structures with High Strength-to-Modulus Ratio. *J. Mater. Sci. Technol.* **2016**, *32*, 505−508.

(28) Bai, Y.; Li, S. J.; Prima, F.; Hao, Y. L.; Yang, R. Electrochemical Corrosion Behavior of Ti-24Nb-4Zr-8Sn Alloy in a Simulated Physiological Environment. *Appl. Surf. Sci.* **2012**, *258*, 4035−4040.

(29) Obbard, E. G.; Hao, Y. L.; Talling, R. J.; Li, S. J.; Zhang, Y. W.; Dye, D.; Yang, R. The Effect of Oxygen on α″ Martensite and Superelasticity in Ti−24Nb−4Zr−8Sn. *Acta Mater.* **2011**, *59*, 112−125.

(30) Zhang, L. C.; Klemm, D.; Eckert, J.; Hao, Y. L.; Sercombe, T. B. Manufacture by Selective Laser Melting and Mechanical Behavior of a Biomedical Ti-24Nb-4Zr-8Sn Alloy. *Scr. Mater.* **2011**, *65*, 21−24.

(31) Wang, K.; Gustavson, L.; Dumbleton, J. The Characterization of Ti−12Mo−6Zr−2Fe. A New Biocompatible Titanium Alloy Developed for Surgical Implants. In *Beta Titanium in the 1990s*;

The Mineral, Metals and Materials Society: Warrendale, Pennsylvania, 1993; pp 2697−2704.

(32) Fanning, J. C. Properties and Processing of a New Metastable Beta Titanium Alloy for Surgical Implant Applications: *TIMETALt 21SRx. Titanium 95′: Science and Technology* **1996**, 1800−1807.

(33) Mishra, A. K.; Davidson, J. A.; Kovacs, P.; Poggie, R. A. Ti−13Nb−13Zr: a New Low Modulus, High Strength, Corrosion Resistant Near-Beta Alloy for Orthopaedic Implants. In *Beta Titanium in the 1990s*; The Mineral, Metals and Materials Society: Warrendale, Pennsylvania, 1993; pp 61−72.

(34) Abdel-Hady Gepreel, M.; Niinomi, M. Biocompatibility of Ti-Alloys for Long-Term Implantation. *J. Mech. Behav. Biomed. Mater.* **2013**, *20*, 407−415.

(35) Saji, V. S.; Choe, H. C.; Brantley, W. A. An Electrochemical Study on Self-Ordered Nanoporous and Nanotubular Oxide on Ti−35Nb−5Ta−7Zr Alloy for Biomedical Applications. *Acta Biomater.* **2009**, *5*, 2303−2310.

(36) Afonso, C. R.; Ferrandini, P. L.; Ramirez, A. J.; Caram, R. High Resolution Transmission Electron Microscopy Study of the Hardening Mechanism Through Phase Separation in a *β*-Ti−35Nb−7Zr−5Ta Alloy for Implant Applications. *Acta Biomater.* **2010**, *6*, 1625−1629.

(37) Yang, K.; Wang, J.; Tang, H.; Li, Y. Additive Manufacturing of In-Situ Reinforced Ti−35Nb−5Ta−7Zr (TNTZ) Alloy by Selective Electron Beam Melting (SEBM). *J. Alloys Compd.* **2020**, *826*, No. 154178.

(38) Kuroda, D.; Niinomi, M.; Morinaga, M.; Kato, Y.; Yashiro, T. Design and Mechanical Properties of New Beta Type Titanium Alloys for Implant Materials. *Mater. Sci. Eng., A* **1998**, *243*, 244−249.

(39) Abdel-Hady, M.; Hinoshita, K.; Morinaga, M. General Approach to Phase Stability and Elastic Properties of *β*-type Ti-Alloys Using Electronic Parameters. *Scr. Mater.* **2006**, *55*, 477−480.

(40) Hennig, R. G.; Trinkle, D. R.; Bouchet, J.; Srinivasan, S. G.; Albers, R. C.; Wilkins, J. W. Impurities Block the *α* to *ω* Martensitic Transformation in Titanium. *Nat. Mater.* **2005**, *4*, 129−133.

(41) Abdel-Hady, M.; Fuwa, H.; Hinoshita, K.; Kimura, H.; Shinzato, Y.; Morinaga, M. Phase Stability Change with Zr Content in *β*-Type Ti−Nb Alloys. *Scr. Mater.* **2007**, *57*, 1000−1003.

(42) Ikehata, H.; Nagasako, N.; Furuta, T.; Fukumoto, A.; Miwa, K.; Saito, T. First-Principles Calculations for Development of Low Elastic Modulus Ti Alloys. *Phys. Rev. B* **2004**, *70*, No. 174113.

(43) Dai, J. H.; Wu, X.; Song, Y.; Yang, R. Electronic Structure Mechanism of Martensitic Phase Transformation in Binary Titanium Alloys. *Int. J. Appl. Phys.* **2012**, *112*, No. 123718.

(44) Raabe, D.; Sander, B.; Friák, M.; Ma, D.; Neugebauer, J. Theory-Guided Bottom-Up Design of *β*-Titanium Alloys as Biomaterials Based on First Principles Calculations: Theory and Experiments. *Acta Mater.* **2007**, *55*, 4475−4487.

(45) Sun, J.; Yao, Q.; Xing, H.; Guo, W. Y. Elastic Properties of *β*, *α″* and *ω* Metastable Phases in Ti−Nb Alloy From First-Principles. *J. Phys.: Condens. Matter.* **2007**, *19*, No. 486215.

(46) Karre, R.; Niranjan, M. K.; Dey, S. R. First Principles Theoretical Investigations of Low Young's Modulus Beta Ti−Nb and Ti−Nb−Zr Alloys Compositions for Biomedical Applications. *Mater. Sci. Eng.* **2015**, *50*, 52−58.

(47) Gutiérrez Moreno, J.; Bönisch, M.; Panagiotopoulos, N. T.; Calin, M.; Papageorgiou, D. G.; Gebert, A.; Lekka, C. E.; et al. Ab-Initio and Experimental Study of Phase Stability of Ti-Nb Alloys. *J. Alloys Compd* **2017**, *696*, 481−489.

(48) Huang, L. F.; Grabowski, B.; Zhang, J.; Lai, M. J.; Tasan, C. C.; Sandlöbes, S.; Raabe, D.; Neugebauer, J. From Electronic Structure to Phase Diagrams: a Bottom-Up Approach to Understand the Stability of Titanium−Transition Metal Alloys. *Acta Mater.* **2016**, *113*, 311−319.

(49) Hu, Q. M.; Li, S. J.; Hao, Y. L.; Yang, R.; Johansson, B.; Vitos, L. Phase Stability and Elastic Modulus of Ti Alloys Containing Nb, Zr, and/or Sn from First-Principles Calculations. *Appl. Phys. Lett.* **2008**, *93*, No. 121902.

(50) Surmeneva, M.; Grubova, I.; Glukhova, N.; Khrapov, D.; Koptyug, A.; Volkova, A.; Surmenev, R. New Ti−35Nb−7Zr−5Ta Alloy Manufacturing by Electron Beam Melting for Medical Application Followed by High Current Pulsed Electron Beam Treatment. *Met.* **2021**, *11*, 1066.

(51) Rechtin, J.; Torresani, E.; Ivanov, E.; Olevsky, E. Fabrication of Titanium-Niobium-Zirconium-Tantalum Alloy (TNZT) Bioimplant Components with Controllable Porosity by Spark Plasma Sintering. *Materials* **2018**, *11*, 181.

(52) Kresse, G.; Hafner, J. Ab Initio Molecular Dynamics for Liquid Metals. *Phys. Rev. B: Condens. Matter Mater. Phys.* **1993**, *47*, 558−561.

(53) Kresse, G.; Furthmüller, J. Efficiency of Ab-Initio Total Energy Calculations for Metals and Semiconductors Using a Plane-Wave Basis Set. *Comput. Mater. Sci.* **1996**, *6*, 15−50.

(54) Kresse, G.; Furthmüller, J. Efficient Iterative Schemes for Ab Initio Total-Energy Calculations Using a Plane-Wave Basis Set. *Phys. Rev. B: Condens. Matter Mater. Phys.* **1996**, *54*, No. 1169.

(55) Kresse, G.; Hafner, J. Norm-Conserving and Ultrasoft Pseudopotentials for First-Row and Transition Elements. *J. Phys.: Condens. Matter* **1994**, *6*, 8245−8257.

(56) Kresse, G.; Joubert, D. From Ultrasoft Pseudopotentials to the Projector Augmented-Wave Method. *Phys. Rev. B: Condens. Matter Mater. Phys.* **1999**, *59*, 1758−1775.

(57) Blöchl, P. E.; Jepsen, O.; Andersen, O. K. Improved Tetrahedron Method for Brillouin-Zone Integrations. *Phys. Rev. B: Condens. Matter Mater. Phys.* **1994**, *49*, 16223−16233.

(58) Perdew, J. P.; Burke, K.; Ernzerhof, M. Generalized Gradient Approximation Made Simple. *Phys. Rev. Lett.* **1996**, *77*, 3865−3868.

(59) Perdew, J. P.; Burke, K.; Ernzerhof, M. Generalized Gradient Approximation Made Simple. *Phys. Rev. Lett.* **1996**, *77*, 1396.

(60) Monkhorst, H. J.; Pack, J. D. Special Points for Brillouin-Zone Integrations. *Phys. Rev. B: Condens. Matter Mater. Phys.* **1976**, *13*, 5188−5192.

(61) Davey, T.; Suzuki, K.; Miura, H.; Chen, Y. Stability and Structural Properties of Vacancy-Ordered and-Disordered ZrC_x. *RSC Advances.* **2021**, *11*, 32573−32589.

(62) Le Page, Y.; Saxe, P. Symmetry-General Least-Squares Extraction of Elastic Data for Strained Materials from Ab Initio Calculations of Stress. *Phys. Rev. B.* **2002**, *65*, No. 104104.

(63) Simmons, G.; Wang, H. *Single Crystal Elastic Constants and Calculated Aggregate Properties: A Handbook* M.I.T. Press: Cambridge, UK, 1971.

(64) Fiorentini, V.; Methfessel, M. Extracting Convergent Surface Energies from Slab Calculations. *J. Phys: Condens. Matter.* **1996**, *8*, 6525−6529.

(65) Henkelman, G.; Arnaldsson, A.; Jónsson, H. A Fast and Robust Algorithm for Bader Decomposition of Charge Density. *Comput. Mater. Sci.* **2006**, *36*, 354−360.

(66) Silvi, B.; Savin, A. Classification of Chemical Bonds Based on Topological Analysis of Electron Localization Functions. *Nature.* **1994**, *371*, 683−686.

(67) Li, C. H.; Hoe, J. L.; Wu, P. Empirical Correlation Between Melting Temperature and Cohesive Energy of Binary Laves Phases. *J. Phys. Chem. Solids.* **2003**, *64*, 201−212.

(68) Anderson, O. L. A Simplified Method for Calculating the Debye Temperature from Elastic Constants. *J. Phys. Chem. Solids.* **1963**, *24*, 909−917.

(69) Wachter, P.; Filzmoser, M.; Rebizant, J. Electronic and Elastic Properties of the Light Actinide Tellu-Rides. *Physica B.* **2001**, *293*, 199−223.

(70) Momma, K.; Izumi, F. VESTA 3 for Three-Dimensional Visualization of Crystal, Volumetric and Morphology Data. *J. Appl. Crystallogr.* **2011**, *44*, 1272−1276.

(71) Pham, M. S.; Dovgyy, B.; Hooper, P. A.; Gourlay, C. M.; Piglione, A. The Role of Side-Branching in Microstructure Development in Laser Powder-Bed Fusion. *Nat. Commun.* **2020**, *11*, No. 749.

(72) Guzmán, J.; de Moura Nobre, R.; Nunes, E. R.; Bayerlein, D. L.; Falcão, R. B.; Sallica-Leva, E.; Landgraf, F. J.; et al. Laser Powder Bed Fusion Parameters to Produce High-Density Ti−53% Nb Alloy

Using Irregularly Shaped Powder from Hydride-Dehydride (HDH) Process. *J. Mater. Res. Technol.* **2021**, *10*, 1372−1381.

(73) Bi, G.; Sun, C. N.; Chen, H. C.; Ng, F. L.; Ma, C. C. K. Microstructure and Tensile Properties of Superalloy IN100 Fabricated by Micro-Laser Aided Additive Manufacturing. *Mater. Des.* **2014**, *60*, 401−408.

(74) Quested, P. N.; McLean, M. Solidification Morphologies in Directionally Solidified Superalloys. *Mater. Sci. Eng.* **1984**, *65*, 171−180.

(75) Xu, J.; Lin, X.; Guo, P.; Dong, H.; Wen, X.; Li, Q.; Xue, L.; Huang, W. The Initiation and Propagation Mechanism of the Overlapping Zone Cracking During Laser Solid Forming of IN-738LC Superalloy. *J. Alloys Compd.* **2018**, *749*, 859−870.

(76) Ikeda, M.; Komatsu, S. Y.; Nakamura, Y. The Effect of Ta Content on Phase Constitution and Aging Behavior of Ti-Ta Binary Alloys. *Mater. Trans.* **2002**, *43*, 2984−2990.

(77) Rossi, M. C.; Ventura, B. N.; Milián, L.; Escuder, A. V.; Amigó Borrás, V. Study of Electrochemical and Biological Characteristics of As-Cast Ti-Nb-Zr-Ta System Based on Its Microstructure. *Met.* **2022**, *12*, No. 476.

(78) Barret, C. S.; Massalski, T. B. *Structure of Metals*; Pergamon Press: Oxford, UK, 1980.

(79) Varin, R. A.; Bystrzycki, J.; Calka, A. Effect of Annealing on the Microstructure, Ordering and Microhardness of Ball Milled Cubic (L12) Titanium Trialuminide Intermetallic Powder. *Intermetallic* **1999**, *7*, 785−796.

(80) Dongol, M.; El-Denglawey, A.; Elhady, A. F.; Abuelwafa, A. A. Structural Properties of Nano 5, 10, 15, 20-Tetraphenyl-21H, 23H-porphine nickel (II) thin films. *Curr. Appl. Phys.* **2012**, *12*, 1334−1339.

(81) Laugier, J.; Bochu, B. *ENSP/Laboratories des Materiaux et du Genie Physique*, BP46.38042; ENSP/Laboratories des Materiaux et du Genie Physique: Saint Martin d'Heres, France, 2000.

(82) Stokes, A. R.; Wilson, A. J. C. The Diffraction of X Rays by Distorted Crystal Aggregates-I. *Proc. Phys. Soc.* **1944**, *56*, 174−181.

(83) Schiavi, A.; Origlia, C.; Germak, A.; Prato, A.; Genta, G. Indentation Modulus, Indentation Work and Creep of Metals and Alloys at the Macro-Scale Level: Experimental iInsights into the Use of a Primary Vickers Hardness Standard Machine. *Materials* **2021**, *14*, 2912.

(84) Toda-Caraballo, I.; Wróbel, J. S.; Dudarev, S. L.; Nguyen-Manh, D.; Rivera-Díaz-del-Castillo, P. E. J. Interatomic Spacing Distribution in Multicomponent Alloys. *Acta Mater.* **2015**, *97*, 156−169.

(85) Pereira, R. M.; Koga-Ito, C. Y.; Rovetta, S. M.; Alcionéia, M.; Henriques, A. R. Bone Tissue Engineering: Production of TNZT Alloy by Powder Metallurgy. *Biointerface Res. Appl. Chem.* **2022**, *12*, 1526−1546.

(86) Sahu, B. R. Electronic Structure and Bonding of Ultralight LiMg. *Mater. Sci. Eng., B* **1997**, *49*, 74−78.

(87) Koval, N. E.; Juaristi, J. I.; Muiño, R. D.; Alducin, M. Elastic Properties of the TiZrNbTaMo Multi-Principal Element Alloy Studied from First Principles. *Intermetallics* **2019**, *106*, 130−140.

(88) Tane, M.; Akita, S.; Nakano, T.; Hagihara, K.; Umakoshi, Y.; Niinomi, M.; Mori, H.; Nakajima, H. Low Young's Modulus of Ti−Nb−Ta−Zr Alloys Caused by Softening in Shear Moduli c′ and c44 Near Lower Limit of Body-Centered Cubic Phase Stability. *Acta Mater.* **2010**, *58*, 6790−6798.

(89) Born, M.; Huang, K. *Dynamical Theory of Crystal Lattices*; Oxford University Press.: Clarendon, UK, 1998.

(90) Tang, B. Y.; Yu, W. Y.; Zeng, X. Q.; Ding, W. J.; Gray, M. F. First-Principles Study of the Electronic Structure and Mechanical Properties of CaMg2 Laves Phase. *Mater. Sci. Eng. A* **2008**, *489*, 444−450.

(91) Luo, X.; Liu, L. H.; Yang, C.; Lu, H. Z.; Ma, H. W.; Wang, Z.; Li, D. D.; Zhang, L. C.; Li, Y. Y. Overcoming the Strength−Ductility Trade-Off by Tailoring Grain-Boundary Metastable Si-Containing Phase in β-Type Titanium Alloy. *J. Mater. Sci. Technol.* **2021**, *68*, 112−123.

(92) Tane, M.; Akita, S.; Nakano, T.; Hagihara, K.; Umakoshi, Y.; Niinomi, M.; Nakajima, H. Peculiar Elastic Behavior of Ti−Nb−Ta−Zr Single Crystals. *Acta Mater.* **2008**, *56*, 2856−2863.

(93) Ji, Z. W.; Hu, C. H.; Wang, D. H.; Zhong, Y.; Yang, J.; Zhang, W. Q.; Zhou, H. Y. Mechanical Properties and Chemical Bonding of the Os−B system: A First-Principles Study. *Acta Mater.* **2012**, *60*, 4208−4217.

▣ Recommended by ACS